Simulation of gross and net erosion of high-*Z* materials in the DIII-D divertor

2016 Nucl. Fusion 56 016021

(http://iopscience.iop.org/0029-5515/56/1/016021)

IOP Publishing | International Atomic Energy Agency Nuclear Fusion

Nucl. Fusion **56** (2016) 016021 (10pp) doi:10.1088/0029-5515/56/1/016021

Simulation of gross and net erosion of high-*Z* materials in the DIII-D divertor

R. Ding[1,2,3], P.C. Stangeby[4], D.L. Rudakov[5], J.D. Elder[4], D. Tskhakaya[6,7], W.R. Wampler[8], A. Kirschner[9], A.G. McLean[10], H.Y. Guo[1,2], V.S. Chan[1] and P.B. Snyder[1]

[1] General Atomics, PO Box 85608, San Diego, CA 92186–5608, USA
[2] Institute of Plasma Physics, Chinese Academy of Sciences, PO Box 1126, Hefei, Anhui 230031, People's Republic of China
[3] Oak Ridge Associated Universities, Oak Ridge, TN# 37831, USA
[4] University of Toronto, Institute for Aerospace Studies, Toronto, M3H 5T6, Canada
[5] University of California San Diego, 9500 Gilman Drive, La Jolla, CA 92093-0417, USA
[6] Fusion@ÖAW, Institute of Applied Physics, TU Wien, Wiedner Hauptstraße 8-10, 1040 Vienna, Austria
[7] Institute for Theoretical Physics, University of Innsbruck, A-6020 Innsbruck, Austria
[8] Sandia National Laboratory, PO Box 5800, Albuquerque, NM 87185, USA
[9] Forschungszentrum Jülich GmbH, Institute of Energy and Climate Research-Plasma Physics, 52425 Jülich, Germany
[10] Lawrence Livermore National Laboratory, 7000 East Avenue, Livermore, CA 94550, USA

E-mail: rding@ipp.ac.cn

Received 3 August 2015, revised 10 November 2015
Accepted for publication 18 November 2015
Published 17 December 2015

Abstract

The three-dimensional Monte Carlo code ERO has been used to simulate dedicated DIII-D experiments in which Mo and W samples with different sizes were exposed to controlled and well-diagnosed divertor plasma conditions to measure the gross and net erosion rates. Experimentally, the net erosion rate is significantly reduced due to the high local redeposition probability of eroded high-*Z* materials, which according to the modelling is mainly controlled by the electric field and plasma density within the Chodura sheath. Similar redeposition ratios were obtained from ERO modelling with three different sheath models for small angles between the magnetic field and the material surface, mainly because of their similar mean ionization lengths. The modelled redeposition ratios are close to the measured value. Decreasing the potential drop across the sheath can suppress both gross and net erosion because sputtering yield is decreased due to lower incident energy while the redeposition ratio is not reduced owing to the higher electron density in the Chodura sheath. Taking into account material mixing in the ERO surface model, the net erosion rate of high-*Z* materials is shown to be strongly dependent on the carbon impurity concentration in the background plasma; higher carbon concentration can suppress net erosion. The principal experimental results such as net erosion rate and profile and redeposition ratio are well reproduced by the ERO simulations.

Keywords: erosion, redeposition, high-*Z* material

(Some figures may appear in colour only in the online journal)

1. Introduction

In fusion experiments, the low-*Z* plasma facing materials (PFM) suffer from strong erosion due to high physical sputtering yield and possibly also chemical erosion processes even under low plasma edge temperatures [1]. The high erosion leading to the built-up of deposits, which can contain large amount of tritium by co-deposition, is responsible for the high long-term tritium inventory in low-*Z* devices [2]. Therefore it is often argued that high-*Z* materials are better PFM for future

fusion devices owing to wall lifetime requirements and the low tritium retention limits. Extensive coverage with high-*Z* PFM has been successfully tested in Alcator C-mod with a molybdenum (Mo) wall [3] and ASDEX-Upgrade with a full tungsten (W) wall [4]. The leading high-*Z* PFM candidate, tungsten, due to its good thermo-mechanical properties, very high sputtering threshold energy and its behaviour under neutron irradiation, has been chosen for the ITER divertor region, which faces the highest particle and energy flux densities [5]. Recent results from JET show that the long-term fuel retention rate with its ITER-like wall (beryllium first wall and tungsten divertor) is dramatically reduced by more than one order of magnitude with respect to the carbon wall [6], although significant problems have been encountered with core levels of W. It has long been known that an intrinsic disadvantage for high-*Z* PFM is that the large core radiation losses due to penetration of high-*Z* impurities may lead to poor plasma performance and restrict plasma operation [7]. Therefore, it is essential to understand and control the impurity source and transport.

The sputter erosion of PFM is normally the source of impurities in the confined plasma. For high-*Z* materials, the most fundamental erosion mechanism is physical sputtering, which occurs when the material surface atoms obtain enough energy from the incident particles to overcome their surface binding energy. Sputtered atoms mostly leave the material surface as neutrals. The neutrals can be ionized when they move through the plasma. After ionization, the movement of impurity ions is influenced by the magnetic and electric fields and by collisions with the plasma ions. The sputtered particles may return to the surface and redeposit there.

The wall lifetime and impurity source are determined by the net erosion of wall materials, which is defined as the difference between gross erosion and redeposition. The net erosion may be considerably reduced by local redeposition of the eroded material, especially for high-*Z* materials, via the so called 'prompt redeposition' effect when the ion Larmor radius is larger than the ionization length, leading to the redeposition during the first gyration [8, 9]. The reduction of net erosion compared to gross erosion has been demonstrated in ASDEX Upgrade [10, 11] and DIII-D [12]. Due to the complex experimental conditions, numerical codes (such as ERO [13] and REDEP/WBC [14]) are needed to simulate the gross and net erosion processes in magnetic confinement devices. The measured campaign-integrated peak net erosion of Mo divertor tiles in Alcator C-MOD was about 10 times higher than that calculated using the REDEP/WBC code, while the simulated gross erosion rate was a reasonable match to that measured by spectroscopy [15]. Further code benchmarking with experiments under well-known conditions continues to be necessary to understand the underlying physics.

In tokamak experiments, passive spectroscopy is a standard method for *in situ* measurements of gross erosion rates using the inverse photon efficiency, the so-called S/XB value, which converts photon fluxes into particle fluxes of eroded atoms [16, 17]. However, the uncertainties of the spectroscopic method are significant. Dedicated experiments have been carried out on DIII-D, in which a novel non-spectroscopic method was used to measure the gross erosion rate [18, 19]. The method is based on post-mortem surface analysis of the net erosion of a sample that is so small that redeposition of the sputtered particles on the sample is negligible. A brief description of the experiments on DIII-D is given in section 2 which provide a very good benchmark for the simulation codes. In section 3, the simulation results using the 3D Monte Carlo code ERO are presented in comparison with experimental results.

2. Experiments at DIII-D

Erosion experiments with high-*Z* materials of molybdenum (Mo) and W were carried out in the lower divertor of the DIII-D tokamak. The experiments are briefly described here; more details can be found in [18, 19]. Thin coatings of Mo or W on a silicon substrate were exposed to well-diagnosed plasma conditions with the divertor material evaluation system (DiMES). The electron density and temperature profiles near the outer strike point (OSP) were measured by the divertor Langmuir probes. The samples were mounted flush with the graphite divertor tiles. L-mode deuterium plasma discharges with lower single null magnetic configuration were used. The OSP was kept near the samples during the plasma current flattop. Figure 1 illustrates the poloidal cross-section of DIII-D with magnetic equilibrium reconstruction of the Mo exposure discharge. The metallic films were deposited in a magnetron sputter deposition system with a carbon inter-layer to prevent the exposure of the silicon substrate to plasma. The coating thickness was measured by Rutherford backscattering (RBS) before and after exposure to determine the net erosion [20]. As shown in figure 2, two different sizes of coated samples were exposed simultaneously, a 1 cm diameter Mo or W film in the centre of the DiMES head and a 1 mm diameter film at 0.5 cm upstream of the 1 cm diameter one. The deposition on one sample from the other sample was negligible. As the ionization mean free path of sputtered neutrals is on the order of mm under the local plasma conditions, very few of the sputtered particles from the 1 mm diameter film would be expected to come back and deposit on the 1 mm spot. Therefore, the measured net erosion rate of the 1 mm diameter sample is treated as approximately the gross erosion rate in the experimental analysis. The ratio of net erosion of 1 cm sample to 1 mm sample can give the net/gross erosion ratio and thus the redeposition ratio for a 1 cm sample. There was a series of similar experiments conducted in DIII-D [18, 19]. In this paper, the most successful experiments on Mo and W erosion with good diagnostic data were selected for detailed modelling analysis. From experimental measurements, the average net erosion rate of Mo is 0.42 nm s^{-1} and the net/gross erosion ratio is 0.56. In W experiments, the average net erosion rate is 0.18 nm s^{-1} with the net/gross erosion ratio of 0.37. The W has a lower net erosion rate but a higher redeposition ratio than Mo.

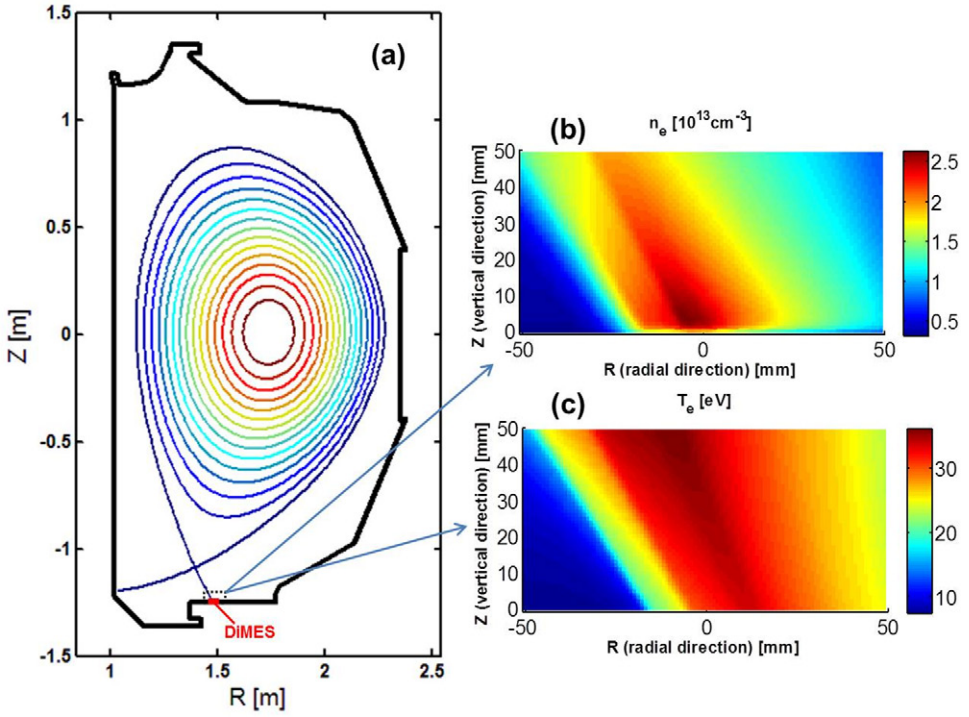

Figure 1. (*a*) EFIT magnetic equilibrium reconstruction of one of the Mo exposure discharges #145672. (*b*) Electron density and (*c*) electron temperature obtained from OEDGE modelling as input for ERO simulation volume indicated by dashed line in (*a*).

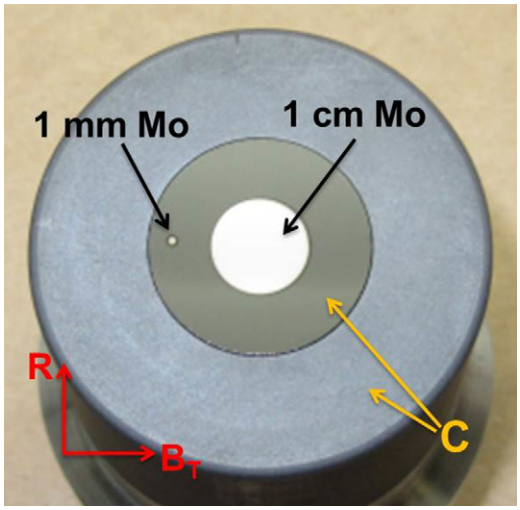

Figure 2. Photograph of the 1 cm and 1 mm Mo samples on the graphite DiMES holder before plasma exposure.

3. Modelling results and discussions

3.1. The ERO code and simulation setup

The 3D Monte Carlo code ERO [13], which simulates the plasma–wall interaction and local impurity transport, is used to model the dedicated DiMES experiments on DIII-D. The code can be divided into two parts: one part calculates the plasma surface interaction including processes of physical sputtering, chemical erosion, reflection and deposition, and the other deals with the transport of impurity particles (neutral or ionized atoms and molecules) in a background plasma by means of the test particle approximation. Particles eroded from the material surface start as neutrals and then can become ionized or dissociated on their way through the plasma. For the impurity ions, the code solves the equation of motion in a magnetic and electrostatic field taking into account the full Larmor gyration of ions. The ion motion along the magnetic field is assumed to be classical, while cross-field motion is specified by an anomalous cross-field diffusion coefficient. Due to the interaction with the plasma background, the originally eroded particles can return to the material surface, where they can be reflected or redeposited and possibly be re-eroded. If a particle is not redeposited it will move back into the plasma as a neutral and be followed again until the particle is redeposited or leaves the simulation volume.

Background plasma parameters are taken as an input and are assumed to be constant during the simulations. For the DiMES simulations, the background plasma is deuterium plasma with carbon impurity due to the full graphite PFM used in DIII-D. The plasma conditions for ERO are provided by the OEDGE code, which uses an Onion Skin Model (OSM) to create the edge plasma solution with the input boundary condition of plasma parameters on divertor targets measured directly by Langmuir probes [21]. For attached L-mode plasmas, OEDGE modelling reproduces the local diagnostic measurements, and therefore, it can reconstruct more realistic local plasma condition close to the material surface than simulations by the normal 2D edge fluid codes, whose boundary conditions are usually imposed at the upstream midpoint of the separatrix. Moreover, the OEDGE simulations run much faster and allow using much higher resolution grid. The plasma density, temperature, flow velocity and electric field on a 2D grid representing the poloidal magnetic structure are obtained by solving the 1D fluid conservation equations along

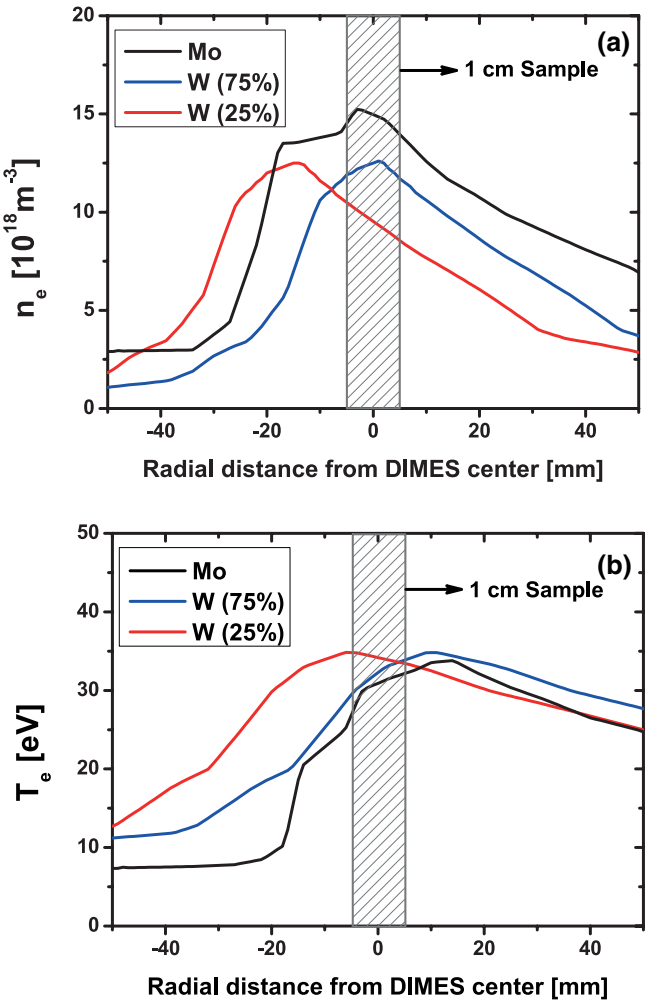

Figure 3. Radial profiles of (*a*) electron density and (*b*) electron temperature measured by the divertor Langmuir probes as OEDGE input for Mo and W exposure experiments.

the magnetic field. The Monte Carlo code EIRENE is used to calculate the hydrogenic source terms [22], which are provided for iteration with OSM until a stable plasma solution is found. Toroidal symmetry is assumed. The 2D distribution of electron density and temperature in radial and vertical direction for ERO simulations on Mo experiments are shown in figure 1. The DiMES centre is at the centre of the simulation volume. Figure 3 shows the radial profiles of electron density and temperature across DiMES from divertor Langmuir probe measurements for Mo and W exposure experiments. During the W experiments, one of the four discharges had a slightly different location of the strike point from the other three discharges. Therefore, modelling of W erosion took into account both plasma parameters with 75% and 25% proportions.

The circular shape of high-*Z* material layer is taken into account in the 3D ERO modelling. The magnetic field is 2.25 T, with the field lines intersecting the divertor surface at a very shallow angle of 1.5°. The anomalous cross field diffusion coefficient is assumed to be 1 m^2 s^{-1}. Physical sputtering by background D and C impurity ions is taken as the main erosion process of high-*Z* materials. The mean charge state of C ions is assumed to be 3. The energy distribution of physically sputtered particles is given by the Thompson distribution around the surface binding energy of 6.83 eV for Mo and 8.68 eV for W. The deposited C on the material surface can be re-eroded by physical and chemical sputtering; the latter is calculated using chemical erosion yields according to the empirical Roth formula [23]. Methane molecules are assumed to be the only chemically eroded species and to have a Maxwellian energy distribution. The break-up of methane into various hydrocarbon species is calculated according to the corresponding reaction rate coefficients [24].

The effect of mixing of C with high-*Z* materials is handled in ERO using a homogenous mixing model [25]. To determine the concentrations of different species in the surface, the surface is divided into an interaction layer and an underlying bulk volume that has an infinite number of substrate particles. The erosion and deposition only take place in the interaction layer with a given thickness. The total number of particles in the interaction layer is kept constant and the different species are distributed homogeneously. The excess number of particles due to net-deposition is moved into the bulk volume according to the relative concentrations of different species inside the interaction layer. Any shortfall in numbers of particles due to net-erosion is filled up with particles from the bulk volume. The interaction layer thickness is determined primarily by the implantation depth of incident particles in the surface. In addition, it must be ensured that in each simulation time step the total number of particles in the interaction layer of a given thickness is larger than the number of eroded particles or deposited particles. The surface reaches steady state composition when the elemental concentrations in the interaction layer do not change anymore with increasing time. It should be noted that the resulting equilibrium concentrations of elements in the interaction layer are independent of the choice of the interaction layer thickness and are determined exclusively by the balance of incoming and outgoing particle fluxes. In the simulations, the thickness of the interaction layer is 10 nm.

First simulations with the ERO code were performed for the Mo erosion experiments. The modelled redeposition ratio of the 1 cm Mo sample was 58%, which is close to the ratio of 54% from previous simulations using the REDEP/WBC code with the same background plasma conditions [26]. Both results are slightly higher than the measured value of 44%. The redeposition ratio for the 1 mm Mo sample from ERO simulation is 16%, which is not a negligible value, thus the net erosion rate of the 1 mm sample cannot be deemed to be the gross erosion rate as assumed in the experimental analysis, and needs a correction. To understand the main driving force of the high redeposition ratio, different assumptions are made in the modelling. When the sheath electric field is assumed to be 0, the modelled redeposition ratio is significantly decreased to 29% for the 1 cm sample and 1.8% for the 1 mm sample. Furthermore, if all the extra forces such as friction force and cross field diffusion are not considered and the redeposition is only due to the gyro motion of particles after ionization, the redeposition ratio is further reduced to 17% for the 1 cm sample and 0.5% for the 1 mm sample. These results indicate that the high redeposition ratio from ERO simulation is dominated by the sheath electric field.

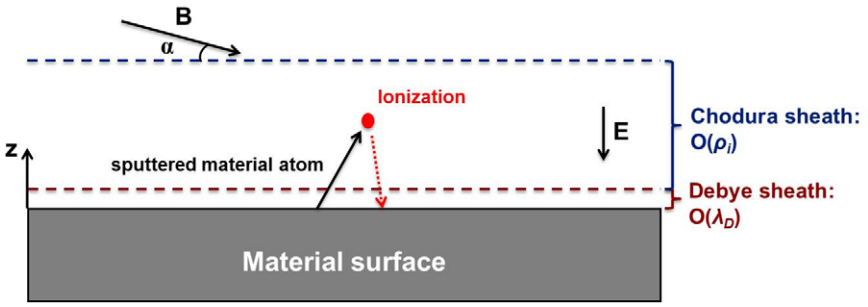

Figure 4. Sketch of the sheath electric field near the material surface in an oblique magnetic field, which dominates the redeposition of sputtered particles.

3.2. Sheath models

When the magnetic field is oblique with respect to the solid material surface, the transition layer between plasma and the material surface consists of a quasi-neutral Chodura sheath with scale length of the order of the ion Larmor radius ρ_i and the Debye sheath of the scale length of several Debye length λ_D (figure 4) [27]. The collisionless fluid model indicates that the parallel flow in the Chodura sheath is deflected by a significant electric field to become nearly normal to the material surface in order to satisfy the classical Bohm condition [28]. The Chodura sheath condition requires that the plasma ion flow velocity along the magnetic field lines at the entrance of the Chodura sheath region has to be greater than or equal to the sound speed. Therefore, an additional plasma pre-sheath is formed upstream of the Chodura sheath where ions are accelerated to sonic velocity. The electric field parallel to the magnetic field existing in plasma pre-sheath is obtained from OEDGE simulations for the ERO modelling of DiMES experiments; it is much weaker than the field perpendicular to the material surface within the Chodura sheath and the Debye sheath. As shown in figure 4, when the sputtered material atoms are ionized within the sheath region, they can be easily drawn back again to the material surface due to the strong electric field.

For a floating surface, the total potential drop across both Chodura sheath and Debye sheath is given approximately by [29]:

$$\Delta\Phi_f = 0.5\frac{kT_e}{e}\ln\left[2\pi\left(\frac{m_e}{m_i}\right)\left(1+\left(\frac{T_i}{T_e}\right)\right)\right], \qquad (1)$$

where T_e, T_i and m_e, m_i are the electron and ion temperature and mass, respectively. Chodura's PIC analysis found that $\Delta\Phi_f$ is approximately independent of the angle between magnetic field line and the surface tangent α [27]; however, the potential drop in the Chodura sheath itself increases with decreasing α. For the case of deuterium plasma and the assumption of $T_e = T_i$, $\Delta\Phi_f = 2.84kT_e/e$. In Brooks' sheath model currently used in the ERO code, the variation of the electrostatic potential in the Debye sheath and Chodura sheath with normal distance from the surface z is taken to be

$$\Phi(z) = \Delta\Phi_f \cdot f \cdot \exp\left(-\frac{z}{2\lambda_D}\right) + \Delta\Phi_f \cdot (1-f) \cdot \exp\left(-\frac{z}{\rho_i}\right) \qquad (2)$$

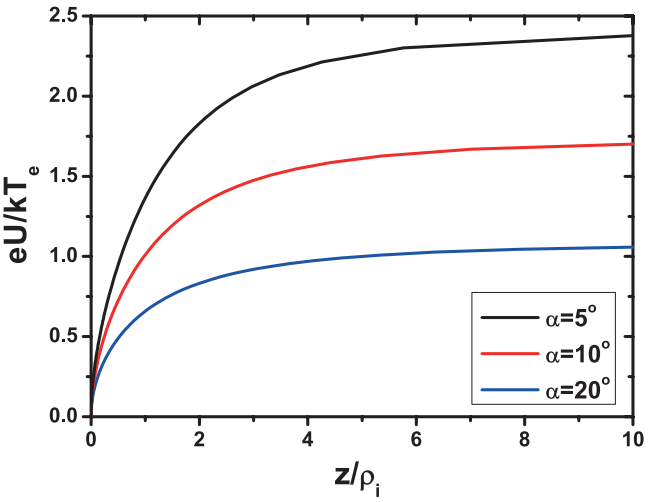

Figure 5. Potential profiles within Chodura sheath in the direction normal to the material surface for several values of α ($z = 0$ is at the Chodura sheath exit).

using a parameter f to define the fraction of sheath potential difference in the Debye region [30]. The quantity f is about 0.2 for the modelling of DIII-D experiments using the Brooks model. It is worthwhile to compare this model with different models based on specific α-dependence of the Chodura sheath.

The collisionless Chodura sheath can be described by the fluid model according to Riemann's analysis [28]. As the quasineutrality condition exists in the Chodura sheath and the electron density is assumed to satisfy the Boltzmann relation, the ion density is given by

$$n_i = n_e = n_{se}\exp\left(\frac{eU}{kT_e}\right), \qquad (3)$$

where n_{se} is the density at the sheath edge (Chodura sheath exit and the Debye sheath entrance). It is assumed that the flow velocity in the direction normal to the material surface v_z reaches the plasma sound speed $c_s = [(kT_e + \gamma kT_i)/m_i]^{1/2}$ at the sheath edge where $U = 0$. An asymptotic solution is obtained with the Chodura sheath entrance at $z \to +\infty$. Figure 5 shows the comparison of potential profiles within the Chodura sheath for different α values from the solutions. The potential drop across the Chodura sheath is $-kT_e/e\ln(\sin\alpha)$, which increases with decreasing α. Assuming the total potential drop across both the Chodura sheath and the Debye sheath is a constant value independent of α, then the Debye sheath may be

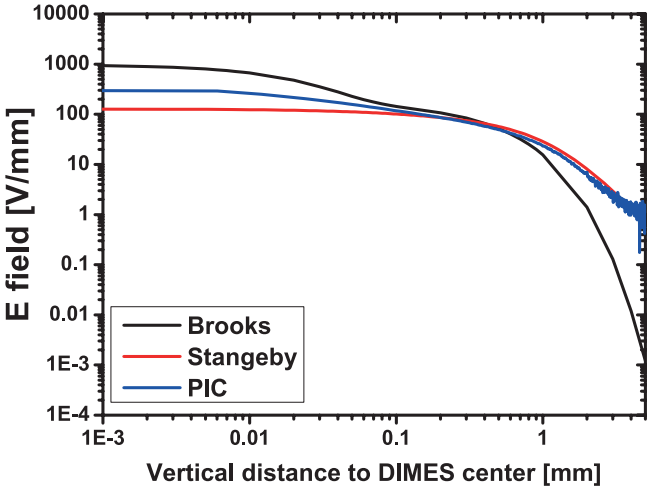

Figure 6. Sheath electric field profiles in the vertical direction from DiMES center obtained from three different sheath models for the modelling of DiMES experiments.

hypothesized to disappear when α is small enough, see the recent analysis by Stangeby [31]. Only the Chodura sheath would then remain and the potential drop would be given by equation (1). In the case of very small α, the potential drop is not sufficient to be able to accelerate the ion flow to reach the sound speed in the direction perpendicular to the material surface at the Chodura sheath exit. From the Boltzmann relation and the ion particle conservation in the Chodura sheath, the Mach number of the plasma flow perpendicular to the material surface at the Chodura sheath exit, instead of being unity, is given by

$$M_{\mathrm{se}\perp} = \exp\left(-\frac{e\Delta\Phi}{kT_\mathrm{e}}\right)\sin\alpha = \left[2\pi\left(\frac{m_\mathrm{e}}{m_\mathrm{i}}\right)\left(1+\left(\frac{T_\mathrm{i}}{T_\mathrm{e}}\right)\right)\right]^{-1/2}\sin\alpha. \quad (4)$$

The sheath electric field from the Stangeby model is compared with that from the Brooks model in the vertical direction from DiMES centre for the DIII-D experimental conditions (figure 6), where it is assumed that $T_\mathrm{e} = T_\mathrm{i} = 31$ eV and $\rho_\mathrm{i} \approx 0.5$ mm. The electric field from the Brooks model is much higher than the Stangeby model near the material surface due to the Debye sheath in the Brooks model, while it becomes much smaller than the Stangeby model away from the material surface.

Kinetic simulations using the particle-in-cell (PIC) method have been carried out for comparison with the analytic approach. The BIT1 electrostatic PIC code with one spatial and three velocity dimensions (1d3v) is used for modelling the sheath close to the DiMES sample [32, 33]. The simulation geometry is a 1D plasma slab bound between two material targets. The total size of the simulated system is 3 cm including two 1 cm sheath regions on both sides and 1 cm source region at the centre. Compared to the half-bounded plasma model, it has advantages that quasineutrality near the source region is self-consistently maintained by the plasma itself and the plasma profiles are monotonic [34]. The edge plasma parameters $n_\mathrm{e} = 1.5 \times 10^{19}$ cm^{-3} and $T_\mathrm{e} = T_\mathrm{i} = 31$ eV are used. Neutral particles and impurities are not taken into account. The motion of ions and electrons is fully resolved in space and time with the Lorentz electromagnetic force as the acting force. The PIC simulation finds that both the Chodura sheath and the Debye sheath exist even when the inclination angle is small. According to the Chodura condition, the Chodura sheath entrance is located at about 5.1 mm from the target surface. The Debye sheath length is about 0.05 mm from the target where quasineutrality is not satisfied any more. The potential drop in the Chodura sheath is about $2.69kT_\mathrm{e}/e$. The comparison of the PIC simulated sheath electric field profile with those from the Brooks model and the Stangeby model is shown in figure 6. The Debye sheath electric field from PIC is much lower than that of the Brooks model, and the Chodura sheath electric field is very close to that of the Stangeby model.

3.3. Redeposition ratio

The sheath electric field profiles from different models have been implemented in the ERO code to compute the Mo and W redeposition ratio. Modelled redeposition ratio of 1 cm Mo sample is 64% for the Stangeby model and 63% for the PIC model, both higher than 58% for the Brooks model and the experimental value. The average ionization mean free path of Mo atoms from ERO modelling is about 1.5 mm, which is smaller than the Chodura sheath width. As shown in figure 6, the larger electric field in the Chodura sheath for the Stangeby model and the PIC model results in the higher redeposition ratio. For 1 mm Mo sample, about 16% of eroded particles are redeposited using all the three models, which is not negligible as well.

In addition to the influence of sheath electric field on redeposition ratio, the distribution of electron density within the Chodura sheath also plays an important role. According to the Boltzmann relation in equation (3), the plasma density drops when approaching the material surface. Since the potential profiles within the Chodura sheath are different for the three models, the spatial variations of density also differ, as shown in figure 7. In the previous ERO simulations, such effects are not taken into account. By imposing the density drop in the ERO simulations, the redeposition ratios for both 1 cm and 1 mm Mo sample are decreased significantly. The main reason is that the average Mo ionization length is increased from 1.5 mm to 2.7 mm (Brooks model), 3.3 mm (Stangeby model) and 3.1 mm (PIC model), respectively. The comparison of redeposition ratios of Mo and W from measurements and modelling using different sheath models is given in table 1. With density variation, the modelled redeposition ratios of 1 cm Mo from the three sheath models are similar and also closer to the experimental value. The Stangeby model and the PIC model give almost the same redeposition ratios due to their similar profiles of electric field and density drop across the Chodura sheath, which are slightly lower than that from the Brooks model due to their lower density profiles. The modelled redeposition ratios of the 1 mm Mo sample also drop to a small value. Note that even better agreement between modelled and measured redeposition ratio is obtained for W. W redeposition ratio is much higher compared to that of Mo, which is mainly due to the shorter ionization mean free path of sputtered W atoms, only about 1 mm. ERO modelling with the Brooks sheath model for 1 cm sample shows that about 75%

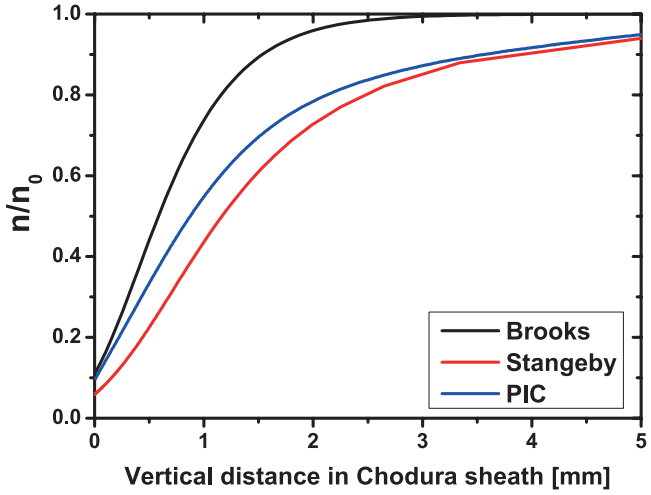

Figure 7. Normalized plasma density profiles within Chodura sheath from three different sheath models for the modelling of DiMES experiments. Plasma density at the Chodura sheath entrance is n_0.

Table 1. Redeposition ratio of Mo and W for 1 cm and 1 mm sample from measurements and ERO modelling using different sheath models. The measured values in brackets are obtained by taking into account the redeposition ratio on 1 mm sample from ERO simulations with the Brooks sheath model.

	Mo		W	
	1 cm	1 mm	1 cm	1 mm
Experiments	44% (46%)		63% (67%)	
ERO (Brooks sheath)	39%	4%	67%	14%
ERO (Stangeby sheath)	35%	3%	63%	9%
ERO (PIC sheath)	36%	3%	63%	9%

of redeposited W is W^+ ions, while 57% of redeposited Mo is Mo^+ ions. As the modelled redeposition ratio of 1 mm W is non-trivial varying from 9% to 14%, the measured redeposition ratio should be corrected for the redeposition occurring on the 1 mm sample. The experimental redeposition ratios of 1 cm Mo and W are then 46% and 67% when the modelled redeposition ratio on 1 mm sample with the Brooks model is used (table 1), which still agree well with the simulation results.

Although, in totality the bounding solid surface to any plasma must float electrically, any part of the solid surface can be non-floating relative to the local plasma. As the redeposition ratio is mainly determined by the Chodura sheath, predictive ERO simulations are also performed for the non-floating material surface. According to the Stangeby sheath model, when the material surface is biased negatively, the Debye sheath may re-appear if the total potential drop is sufficiently large. Conversely, if the total potential drop is decreased to less than the floating potential drop, only the Chodura sheath is hypothesized to exist. If the total floating potential drop $\Delta\Phi$ is reduced by some factor, the standard Mach number of the plasma flow at the Chodura sheath exit $M_{se\perp}$ is then decreased and can be calculated by equation (4). The potential profile within the Chodura sheath can be computed by solving fluid

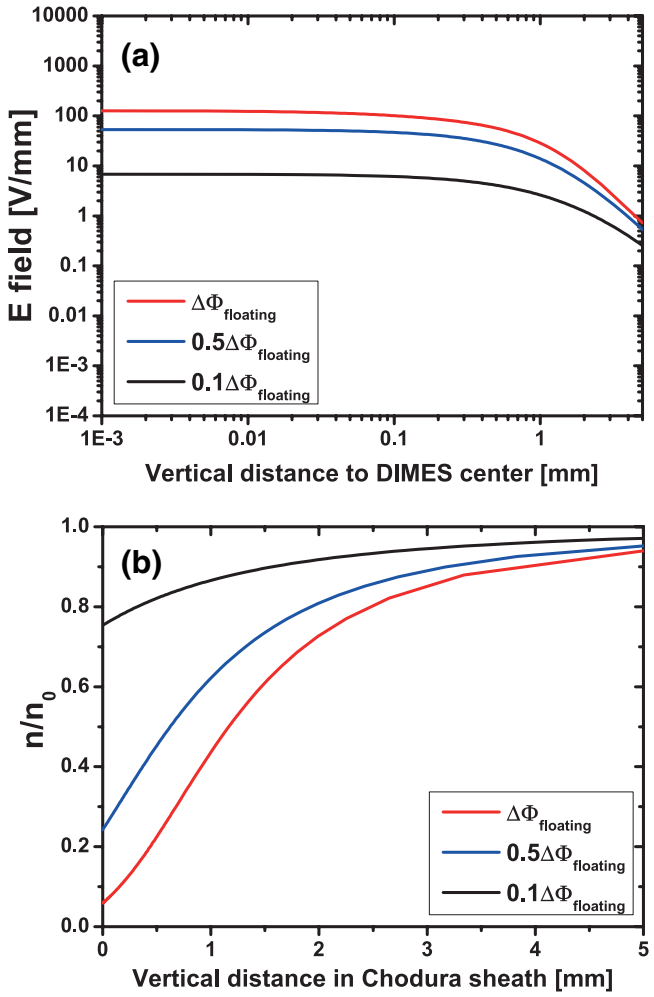

Figure 8. Profiles of (*a*) electric field and (*b*) normalized plasma density across Chodura sheath for different total potential drop.

equations [31]. When the total potential drop is reduced to a fraction of the floating potential, the sheath electric field is decreased but the density becomes larger within the Chodura sheath, as shown in the figure 8. Both of these have opposite effects on the redeposition ratio. In figure 9, the dependence of modelled redeposition ratio of the 1 cm Mo and W samples on total sheath potential drop is given. When the sheath potential drop is reduced, the redeposition ratios of Mo and W show an even slight increase owing to the higher electron density. As the total potential drop is reduced to a tenth of the floating potential drop, the redeposition ratios of Mo and W still remain almost invariant. Note that decreasing the total potential drop may reduce the gross erosion rate because the sputtering yield can be decreased due to the lower ion incident energy. For example, the sputtering yield of W by C^{3+} ion incidence is reduced by more than an order of magnitude when decreasing the sheath potential by a factor of 10 under the DiMES experiment conditions. As the redeposition ratio of W is not reduced, the net erosion rate will decrease by the same factor as gross erosion rate. Therefore, decreasing the potential drop across the sheath can significantly suppress both gross and net erosion rate of high-*Z* materials.

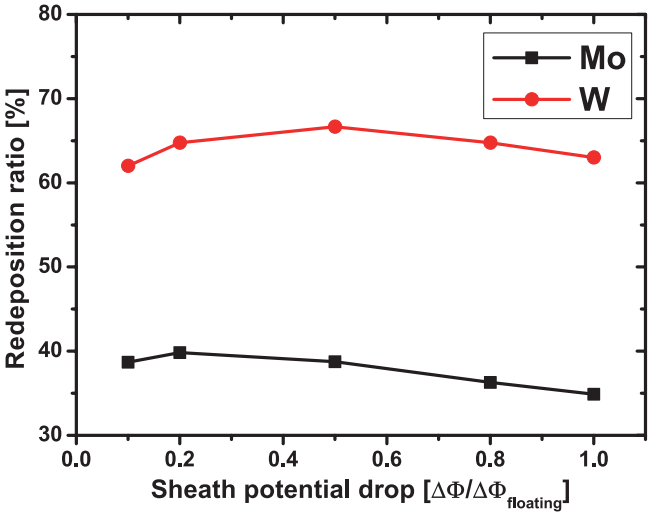

Figure 9. ERO modelled redeposition ratio of the 1 cm Mo and W samples as a function of total sheath potential drop using the Stangeby sheath model.

3.4. Net erosion

As the three sheath models result in similar results, the net erosion rates of 1 cm Mo and W sample was then simulated using the Brooks sheath model for comparison with experiments. An important input parameter for the modelling that influences the net erosion rate is the concentration of the carbon impurity in the background plasma, which originates from the graphite plasma-facing components in DIII-D. The carbon impurity content not only influences the sputtering rate of the high-Z materials, but also can change the overall erosion and deposition balance on the material surface.

The carbon concentration in the background plasma was not measured in the experiments. Therefore, Mo net erosion rate was simulated assuming different carbon concentration from 1% to 2% (figure 10). The net erosion rate is strongly dependent on the carbon impurity concentration. Initially in ERO simulations, the physical sputtering rate is high for the pure Mo surface. Higher carbon concentration leads to more carbon deposition in the mixed material surface layer, which reduces the effective sputtering rate of Mo due to surface dilution. The carbon ratio in the surface interaction layer is determined by the erosion and deposition flux balance of carbon, which becomes constant when steady state is reached in the simulation. Further increasing the carbon concentration in the plasma can even put the surface into a net deposition condition. These results agree with the recent experiments in DIII-D in which Mo net erosion is significantly suppressed by the local methane gas injection leading to the higher local carbon impurity level in the plasma [35]. ERO modelled Mo net erosion rate was 0.43 nm s^{-1} assuming a carbon concentration of 1.8%, which reproduces well the experimental value of 0.42 nm s^{-1}. If the same carbon concentration is assumed for W experiments, the net erosion rate is 0.14 nm s^{-1} from modelling also close to the measured value of 0.18 nm s^{-1}. Although the carbon ratio in the W surface interaction layer is lower than the Mo surface layer because of the higher carbon reflection coefficient on W, the W net erosion rate is still much

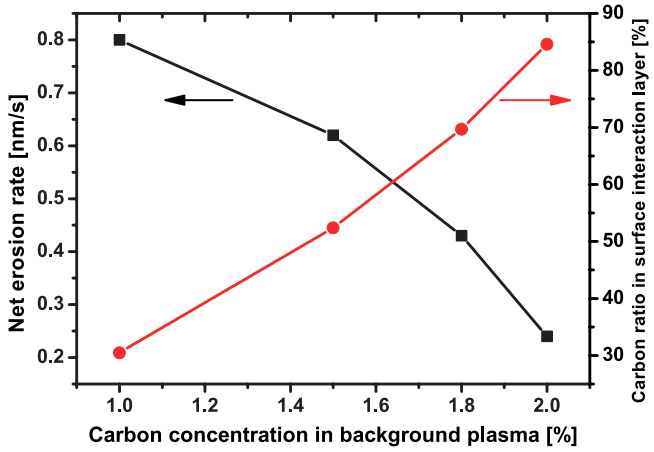

Figure 10. ERO modelled net erosion rate of the 1 cm Mo sample and the carbon ratio in surface interaction layer as a function of carbon concentration in the background plasma.

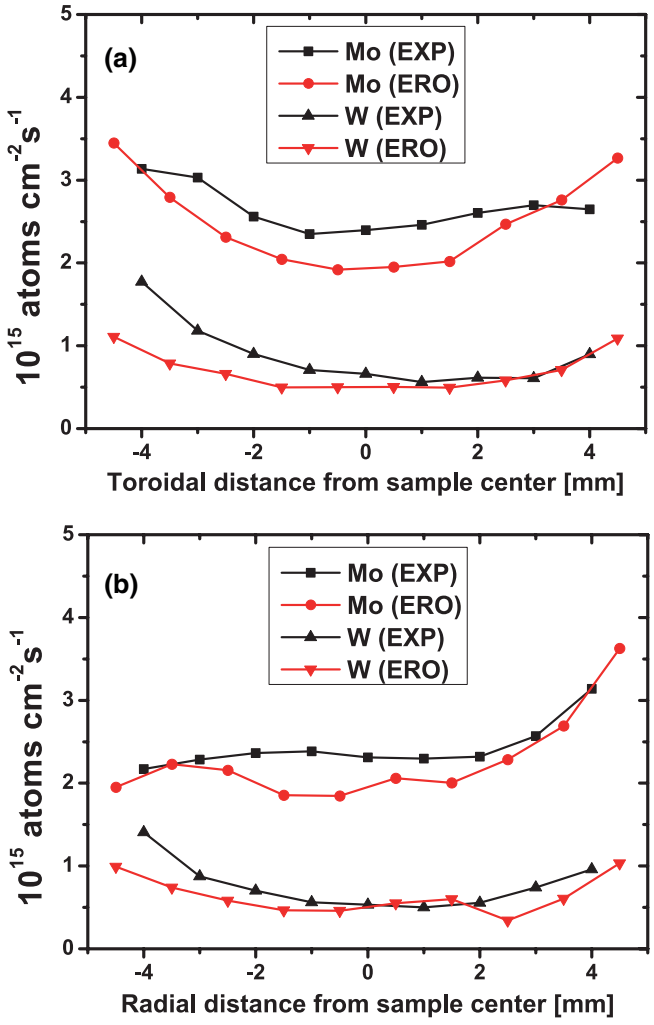

Figure 11. Comparison of toroidal (a) and radial (b) profiles of net erosion rates for 1 cm Mo and W samples between the experiments (EXP) and modelling (ERO).

lower than Mo due to its lower sputtering yield and higher redeposition ratio.

Figure 11 shows the measured spatial distributions of net erosion rate for 1 cm Mo and W in comparison with the

modelling. The modelled results are in good agreement with the experiments in both toroidal and radial direction. As seen in figure 11, the net erosion rate is lower at the centre of the sample than near the edge, which is due to higher redeposition at the centre from neighbouring areas. As the redeposition of high-*Z* materials is dominated by sheath electric field, the influence of parallel transport along the magnetic field line on the redeposition is not significant. Therefore, almost symmetric net erosion profile in the toroidal direction is obtained from the modelling. Modelling shows that the radial dependence of Mo net erosion rate is mainly determined by the local carbon ratio in the surface layer. The radial variation of plasma density and temperature leads to higher carbon content at the outboard edge surface layer in equilibrium. The influence of the carbon ratio in the surface layer on W net erosion rate is much weaker.

4. Summary

Gross and net erosion of high-*Z* materials Mo and W in dedicated DIII-D DiMES experiments have been modelled using the 3D Monte Carlo code ERO. The background plasma parameters in ERO are based on the output from simulations using the OEDGE code calibrated with Langmuir probe data. The net erosion of high-*Z* materials is significantly reduced by local redeposition compared to gross erosion. According to the ERO simulation results, the redeposition ratio is mainly determined by the electric field and the plasma density drop in the Chodura sheath. A new sheath model for small angles between the magnetic field and the material surface (e.g. 1.5°) that involves disappearance of the Debye sheath is compared with a standard sheath model and kinetic (PIC) simulations. Similar redeposition ratios were obtained from ERO modelling using the three models due to similar ionization lengths, all being close to the measured values. Modelling also shows that if the potential drop across the sheath decreases, the redeposition ratio is not reduced due to the higher density profile in the Chodura sheath. This means that decreasing sheath potential, e.g. via biasing may not only suppress gross erosion due to lower incident energy, but also net erosion due to the high redeposition ratio. Net erosion rates are also computed with the assumption of different carbon concentration in the background plasma using a homogeneous material mixing model. Higher carbon concentration leads to more carbon in the surface interaction layer, and thus lower net erosion rate of metal. With a carbon concentration of 1.8%, the modelled net erosion rates of Mo and W are in good agreement with the measured erosion rates. The net erosion profiles on the two samples in both toroidal and poloidal direction are well reproduced by ERO simulations.

Although current studies were carried out for specific divertor plasma conditions (low density, high temperature, no ELMs), it provides a good benchmark for the ERO modelling and helps to understand the key physics of erosion and deposition in tokamaks. Further code benchmarking should be extended to different experiments with other geometries and plasma conditions. The redeposition of high-*Z* materials has a critical effect on high-*Z* impurities level in the plasma, which should be taken into account carefully in the modelling of global impurity source and transport. Such analysis can also help to find new solutions to suppress the erosion of materials in tokamaks.

Acknowledgments

This material is based upon work supported by the US Department of Energy, Office of Science, Office of Fusion Energy Sciences and Office of Advanced Scientific Computing Research through the Scientific Discovery through Advanced Computing (SciDAC) project on Plasma-Surface Interactions, using the DIII-D National Fusion Facility, a DOE Office of Science user facility, under Awards DE-FC02-04ER54698, DE-FG02-07ER54917, and DE-AC52-07NA27344. DIII-D data shown in this paper can be obtained in digital format by following the links at https://fusion.gat.com/global/D3D_DMP. Sandia National Laboratories is a multi-program laboratory managed and operated by Sandia Corporation, a wholly owned subsidiary of Lockheed Martin Corporation, for the US Department of Energy's National Nuclear Security Administration under contract DE-AC04-94AL85000. The first author acknowledges the supports by the National Magnetic Confinement Fusion Science Program of China under contract Nos 2013GB107004, the National Natural Science Foundation of China under Contract Nos 11375010, and the Sino-German Center for Research Promotion under Contract No GZ769. D. Tskhakaya acknowledges the support by the project FWF P26544-N27.

References

[1] Roth J. *et al* 1996 *Nucl. Fusion* **36** 1647
[2] Roth J. *et al* 2008 *Plasma Phys. Control. Fusion* **50** 103001
[3] Lipschultz B. *et al* 2001 *Nucl. Fusion* **41** 585
[4] Kallenbach A. *et al* 2005 *Plasma Phys. Control. Fusion* **47** B207
[5] Pitts R.A. *et al* 2013 *J. Nucl. Mater.* **438** S48
[6] Brezinsek S. *et al* 2013 *Nucl. Fusion* **53** 083023
[7] Suckewer S. and Hawryluk R.J. 1978 *Phys. Rev. Lett.* **40** 1649
[8] Naujoks D. *et al* 1996 *Nucl. Fusion* **36** 671
[9] Chankin A.V. *et al* 2014 *Plasma Phys. Control. Fusion* **56** 025003
[10] Krieger K. *et al* 1999 *J. Nucl. Mater.* **266–269** 207
[11] Dux R. *et al* 2009 *J. Nucl. Mater.* **390–391** 858
[12] Wampler W.R. *et al* 1996 *J. Nucl. Mater.* **233–237** 791
[13] Kirschner A. *et al* 2000 *Nucl. Fusion* **40** 989
[14] Brooks J.N. 2002 *Fusion Eng. Des.* **60** 515
[15] Brooks J.N. *et al* 2011 *J. Nucl. Mater.* **415** S112
[16] Van Rooij G.J. *et al* 2013 *J. Nucl. Mater.* **438** S42
[17] Brezinsek S. *et al* 2011 *Phys. Scr.* **T145** 014016
[18] Stangeby P.C. *et al* 2013 *J. Nucl. Mater.* **438** S309
[19] Rudakov D.L. *et al* 2014 *Phys. Scr.* **T159** 014030
[20] Wampler W.R. *et al* 2013 *J. Nucl. Mater.* **438** S822
[21] Stangeby P.C. *et al* 2003 *J. Nucl. Mater.* **313–316** 883
[22] Reiter D. *et al* 2002 *Plasma Phys. Control. Fusion* **44** 1723
[23] Roth J. *et al* 2005 *J. Nucl. Mater.* **337–339** 970
[24] Ding R. *et al* 2009 *Plasma Phys. Control. Fusion* **51** 055019
[25] Kirschner A. *et al* 2009 *J. Nucl. Mater.* **390–391** 152
[26] Brooks J.N. *et al* 2013 *J. Nucl. Mater.* **438** S673

[27] Chodura R. 1982 *Phys. Fluids* **25** 1628
[28] Riemann K. U 1994 *Phys. Plasmas* **1** 552
[29] Stangeby P.C. 2000 *The Plasma Boundary of Magnetic Fusion Devices* (Bristol: Institute of Physics Publishing)
[30] Brooks J.N. 1990 *Phys. Fluids* B **2** 1858
[31] Stangeby P.C. 2012 *Nucl. Fusion* **52** 083012
[32] Tskhakaya D. *et al* 2011 *J. Nucl. Mater.* **415** S860
[33] Tskhakaya D. *et al* 2007 *J. Comput. Phys.* **225** 829
[34] Tskhakaya D. *et al* 2005 *Plasma Phys. Control. Fusion* **47** A327
[35] Rudakov D.L. *et al* 2015 *J. Nucl. Mater.* **463** 605